Core-level binding energy shifts in ultrathin alkali-halide films on metals: KCl on Ag(100)

Séverine Le Moal, Ina Krieger, Roman Kremring, Simon Weiß, Xiaosheng Yang, Serguei Soubatch, F. Stefan Tautz, Mathieu Silly, Andrei Borisov, Moritz Sokolowski, et al.

Core-level binding energy shifts in ultrathin alkali-halide films on metals: KCl on Ag(100)

Séverine Le Moal,[†] Ina Krieger,[‡] Roman Kremring,[‡] Simon Weiß,[¶,§] Xiaosheng Yang,[¶,§] Serguei Soubatch,[¶,§] F. Stefan Tautz,[¶,§,‖] Mathieu Silly,[⊥] Andrei G. Borisov,[†] Moritz Sokolowski,[‡] and Eric Le Moal[*,†]

†*Université Paris-Saclay, CNRS, Institut des Sciences Moléculaires d'Orsay, 91405, Orsay, France*

‡*Institut für Physikalische und Theoretische Chemie der Universität Bonn, Wegelerstrasse 12, 53115 Bonn, Germany*

¶*Peter Grünberg Institut (PGI-3), Forschungszentrum Jülich, 52425 Jülich, Germany*

§*Jülich Aachen Research Alliance (JARA)-Fundamentals of Future Information Technology, 52425 Jülich, Germany*

‖*Experimental Physics IV A, RWTH Aachen University, 52074 Aachen, Germany*

⊥*Synchrotron-SOLEIL, Saint-Aubin, BP48, F91192 Gif sur Yvette Cedex, France*

E-mail: eric.le-moal@universite-paris-saclay.fr

Phone: +33 (0)1 69 15 66 97. Fax: +33 (0)1 69 15 67 77

Abstract

We present an experimental and theoretical analysis of the core-level binding energy shifts in metal-supported ultrathin KCl films, i.e., a case from a broader class of few-atom-thick, wide-bandgap insulating layers that is increasingly used in nanosciences and nanotechnologies. Using synchrotron-based high-resolution photoemission spectroscopy (HRPES) measurements, we identify the different contributions to the core-level binding energy shifts for the Cl^- anions and K^+ cations of two to three atomic layer-thick KCl films grown on Ag(100). The distances of the Cl^- and K^+ ions of the first two atomic layers of the KCl film from the metal substrate are determined from normal incidence X-ray standing wave measurements. We also calculate the core-level binding energy shifts using an analytical electrostatic model and find that the theoretical results are in agreement with the experimental HRPES results only when polarization and substrate-induced image charge effects are taken into account. Finally, our results evidence the effect of the third atomic layer of the KCl film, which partially covers and screens the first two atomic layers of KCl wetting the metal substrate.

Introduction

Alkali halides (AH) are naturally abundant ionic crystals, which are increasingly used as ultrathin insulating layers in nanosciences and nanotechnology. This is because, on the one hand, AH films as thin as two or three atomic layers already exhibit a wide, bulk-like, electronic bandgap.[1,2] On the other hand, such films can be grown through simple techniques, such as thermal evaporation from a crucible, on a variety of metal[3–12] and semiconductor[13–18] surfaces. Ultrathin AH films epitaxially grown on metals have been key in recent breakthroughs in scanning probe microscopy experiments in nanophysics and nanooptics, to probe and control the states of individual atoms and molecules electronically decoupled from their substrate.[19–28] AH thin films are also increasingly used as electronic buffer layers at the electrode/semiconductor interfaces of organic-based optoelectronic devices, to engineer the

band-bending effects at these interfaces and thus to optimize the device performance.[29–36] In such applications, understanding the effects of the atomic-scale structure, low dimensionality, and interfacial interactions of the insulating layer on its electronic properties is crucial. Such effects are associated with core-level binding energy shifts, which can be measured using photoemission spectroscopy. In particular, the differences in core-level binding energy between the atoms at the surface and the atoms in the bulk have been studied for various materials,[37–41] also including AHs.[42,43] However, for ultrathin AH films, the record on core-level binding energy shifts is very scarce.[44,45]

In general, core-level binding energy shifts result from a change in both the initial and final states of the photoemission process. In ionic insulators, the initial state where an electron is localized on an ion at the crystal lattice site may shift in energy due to a modification of the Madelung potential, e.g., surface ions have a different coordination number as compared to the bulk.[42] In the final state of photoemission, the hole created by the removal of an electron from the crystal is screened by the polarization of the neighboring ions in the lattice, which is also dependent on their atomic coordination. Moreover, in the case of adsorbed species and supported thin films, the energy of the initial and final states are both modified by the substrate polarization effects. The substrate polarization is often described using model approach based on the electrostatic screening, such as e.g. method of the image charges.[38,46–49]

Recently, a new aspect of core-level binding energy shifts in supported manganese oxide (MnO) overlayers has been reported,[50] which may be extended to ultrathin AH films, given that both MnO and AHs are ionic insulators. The authors modeled the core-level photoemission line shapes of few atomic layer-thick MnO(100) films grown on Au(111) as a superposition of contributions from interior, terrace and edge atoms, i.e., atomic sites of different coordination geometry. They predicted the core-level binding energy for these three types of atomic sites, based on analytical calculations of the Madelung potential and the polarization effects. Such an analysis of photoemission spectra unravels the statistical

distribution of the different atomic sites in a thin film, which is key for applications, e.g., in heterogeneous catalysis. So far, such an analysis for ultrathin AH films has not been reported.

In previous works, the core-level and Auger electron photoemission line shapes of the alkali-metal cation in AH thin films on metals have been tentatively decomposed into first-layer, second-layer and multilayer contributions[45] as well as interfacial, bulk and surface contributions.[44] However, these decompositions were not accompanied with calculations of the theoretical binding energy shifts. Moreover, in these studies, the core-level binding energy shift for the halide anion either was not observed or was considered negligible for the surface ions of bulk AH crystals.[42] As recently pointed out for metal oxide thin films,[41] erroneous approximations or assumptions may lead to flawed interpretations of the core-level binding energy shifts and a wealth of information that they contain about the physical and chemical properties of low-dimensionality systems such as ultrathin films may be lost. Thus, the question naturally arises as to whether the core-level binding energy shifts of ultrathin AH films on metals could be modeled using analytical calculations of the Madelung potential and the polarization effects. We attempt to address this question in the present contribution.

In this paper, combining experiment and theory, we investigate how the electrostatic screening by the metal substrate and the polarization of the ionic lattice affect the core-level binding energies of the Cl anions and K cations of ultrathin potassium chloride (KCl) films grown on Ag(100). Figure 1 shows a schematic view of the experiment. Two to three atomic layer-thick KCl islands are grown on Ag(100) in ultrahigh vacuum (UHV) and the Cl $2p$ and K $2p$ core level energies are measured using synchrotron-based high-resolution photoemission spectroscopy (HRPES). The vertical distances of the ions in the first and second atomic layers of KCl from the top Ag(100) atoms are retrieved using the normal-incidence X-ray standing wave (NIXSW) technique.[51] Based on analytical calculations, we determine the relative contributions of the image charge and polarization effects to the observed binding energy shifts.

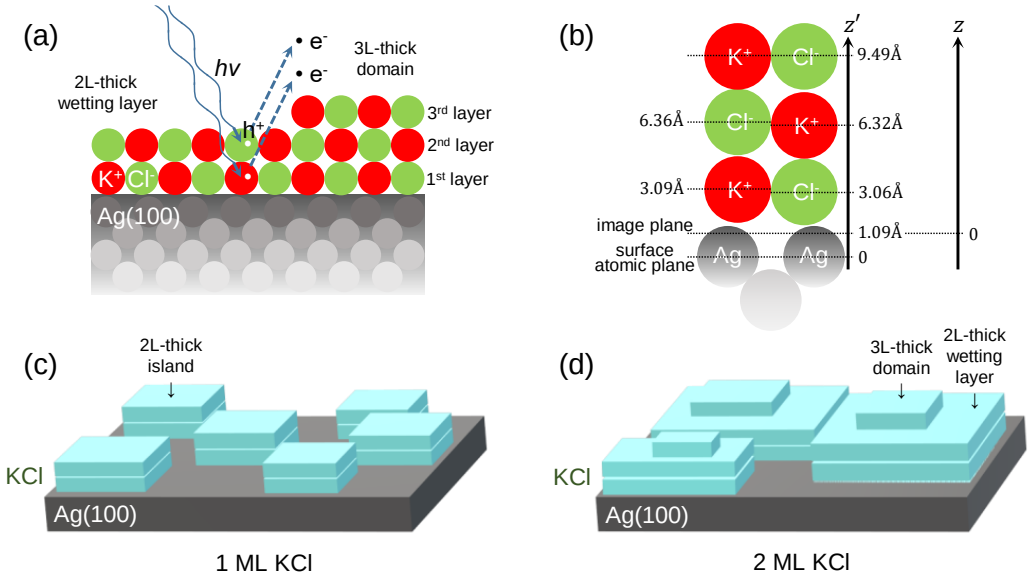

Figure 1: (a) Schematic view of the photoemission experiment on a two atomic layer (2L)-thick KCl film on Ag(100), featuring a three atomic layer (3L)-thick domain. $h\nu$, e^- and h^+ stand for the incident X-ray photons, the photoemitted electrons and the resulting holes in the core levels of the ions, respectively. (b) Vertical distances of the Cl^- and K^+ ions in the different layers from the metal substrate, as considered in the theoretical model. These distances are experimentally determined using NIXSW for the first two KCl layers and theoretically estimated using the lattice parameter of bulk KCl for the third KCl layer. In the text, z and z' are defined as the vertical distances from the Ag(100) image plane and surface atomic plane, respectively. (c,d) Schematic view of the proposed KCl film morphology for deposited amounts of KCl corresponding to (c) one and (d) two monolayers (1 and 2 ML).

Experimental methods

The surface of an Ag(100) single crystal was cleaned by sputtering (Ar ions, 700 eV) and annealing cycles (at 773 K) and its quality was checked using low energy electron diffraction. For all HRPES measurements, ultrathin KCl films were grown in UHV by thermal evaporation from a crucible heated at 793 K and adsorption on the Ag(100) crystal kept at room temperature. We used $\geq$ 99.9995%-pure KCl purchased from Sigma Aldrich and a temperature-controlled evaporator from Kentax. The deposition rate ($\approx$ 0.2 Å min^{-1}) was determined using a calibrated quartz microbalance and the amount of deposited KCl was controlled via the deposition time. In the following, we express the amount of deposited KCl in number of monolayers (ML), i.e., as the "nominal" thickness of the film. As a definition, 1 ML of KCl is deposited on the substrate when the density of atoms in the KCl film per unit area equals that of the (100) atomic plane of bulk KCl. The nominal thickness of the KCl films prepared for the HRPES experiments is 1 ML and 2 ML, respectively.

The core-level HRPES measurements were carried out at the TEMPO beamline of the SOLEIL synchrotron facility (Saint-Aubain, France), using a high-energy-resolution Scienta SES2002 photoelectron analyzer equipped with a delay-line detector. The accessible energy range at the TEMPO beamline is from 50 to 1500 eV and the maximum resolving power is $E/\Delta E > 10000$.[52] The analyzer was operated in the constant-pass-energy mode (20 eV) and the energy step was 25 meV for K 2p and Cl 2p core-level regions. The sample was cooled down to about 120 K during all HRPES measurements. The preparation of the sample and the HRPES measurements were carried out in two connected UHV chambers. The base pressure in both chambers was $< 3 \times 10^{-10}$ mbar. We used the CasaXPS software for the HRPES peak fitting. The background caused by inelastically scattered photoelectrons was modeled using a Shirley baseline. The core-level peaks were fitted using the product of a Gaussian and a Lorentzian (i.e., a pseudo-Voigt function), with the Gaussian and the Lorentzian contributing 70% and 30% to the peak width, respectively (i.e., the GL(30) function in CasaXPS).

The NIXSW experiments[51] were performed at the I09 beamline of the Diamond Light Source synchrotron facility (Oxfordshire, UK), on ultrathin KCl films grown on Ag(100) at 200 K. The measurements were carried out at energies close to the Ag(200) Bragg energy (3.035 keV) and the K $2p$ and Cl $2p$ levels were recorded using angular integrated detection of the photoelectrons. During the NIXSW measurements, the sample was kept at about 230 K. The K$2p$ and Cl$2p$ spectra were fitted by two doublets composed each of two lines with a pseudo-Voigt profile of equal full width at half maximum (FWHM). The area ratio of the two components of the doublet was constrained to 2. The coherent fractions and positions were determined from the respective yield curves using the program Torricelli.[53] We did not take into account non-dipolar correction parameters in the fit of the K$2p$ and Cl$2p$ spectra, because these parameters are not well-established for $2p$ orbitals.[51]

Theoretical methods

To analyze the experimental data and to elucidate the observed trends, we use an analytical model based on the earlier developments for the description of the bulk and surface core-level shifts in ionic solids[54–57] and for the description of the polarization effects in molecular adlayers deposited on metal substrates.[48,58,59] More details on the model can be found in Ref.[60] In brief, we construct the lattice of ionic crystal films using large neutral supercells consisting of halide anions and alkali-metal cations. In this way, the asymptotic electrostatic potential of each supercell is given by the high-order multipole, which ensures the fast convergence of the Madelung potential. The experimentally measured core-level binding energy shift of the cation or anion located at a given lattice site j_h of the KCl film corresponds to the difference in the work needed to bring the hole from infinity to this particular ion either located in vacuum or embedded in the ionic lattice. It can be approximated by the potential created by the rest of the system (ion crystal film and metallic substrate) at the KCl lattice site j_h with position vector $\mathbf{R}_{j_h}$ in response to the +1 charge placed at the same lattice site. Using

atomic units, this energy shift can be expressed as

$$\Delta E = \sum_{j \neq j_h} q_j \left|\mathbf{R}_j - \mathbf{R}_{j_h}\right|^{-1} + \sum_j \tilde{q}_j \left|\tilde{\mathbf{R}}_j - \mathbf{R}_{j_h}\right|^{-1} - \frac{1}{4z_{j_h}} + \frac{1}{2}\sum_{j \neq j_h}\left[\mathcal{U}(\mathbf{R}_{j_h} - \mathbf{R}_j, \mathbf{p}_j) + \mathcal{U}(\mathbf{R}_{j_h} - \tilde{\mathbf{R}}_j, \tilde{\mathbf{p}}_j)\right], \quad (1)$$

The first two sums in Eq. 1 describe the point charge interactions (i.e., the Madelung potential). We account for the field screening by the metal substrate, resulting in image potential interactions with $\tilde{q}_j = -q_j$ being the electrostatic image of the charge q_j of the lattice site j with position vector $\mathbf{R}_j$. The image charge $\tilde{q}_j$ is located at $\tilde{\mathbf{R}}_j = \mathbf{R}_j - 2\hat{e}_z(\hat{e}_z \cdot \mathbf{R}_j)$, where $\hat{e}_z$ is the unit length vector along the z-axis. We consider Cartesian coordinates with z-axis perpendicular to the surface atomic plane of Ag(100) and pointing into the vacuum. The origin of z-coordinates corresponds to the Ag(100) image plane defined with $(x, y, z = 0)$. It is located in the vacuum region at $z' = 1.09$ Å (2.06 atomic units[61]) above the surface atomic plane of Ag(100), as shown in Fig. 1(b). The second and third terms in Eq. 1 stand for the interaction of the hole with electrostatic image of the charge q_j, and with its own electrostatic image, where $z_{j_h} = \hat{e}_z \cdot \mathbf{R}_{j_h}$.

Finally, the last sum in Eq. 1 accounts for the polarization (i.e., the Mott-Littleton) effect. The field of the hole located at $\mathbf{R}_{j_h}$ polarizes the ionic crystal. Thus, the hole interacts with dipoles $\mathbf{p}_j$ induced at the rest of the ionic sites $j \neq j_h$ of the KCl film, and with their images as $\tilde{\mathbf{p}}_j = -\mathbf{p}_j + 2\hat{e}_z(\hat{e}_z \cdot \mathbf{p}_j)$. Since this is the self-interaction, the corresponding potential terms enter Eq. 1 with factor $\frac{1}{2}$. The dipole potential $\mathcal{U}$ is given by $\mathcal{U}(\mathbf{r}, \mathbf{p}) = \left[3(\mathbf{p} \cdot \mathbf{r})\mathbf{r} - \mathbf{p}\ \mathrm{r}^2\right]/\mathrm{r}^5$, where $\mathrm{r} = |\mathbf{r}|$ and $\mathbf{r}$ is the position vector. The dipoles induced at the lattice sites of the ionic film are determined from $\mathbf{p}_j = \alpha_j\ \mathbf{E}_j$, where α_j is the polarizability of the $Cl^-(K^+)$ ion located at the site j, and $\mathbf{E}_j$ is the local field at this site induced by the presence of the hole at $\mathbf{R}_{j_h}$. For ionic polarizabilities, we use values reported by Jaswal and Sharma[62] (i.e., 2.95 Å^3 for Cl^- and 1.13 Å^3 for K^+). Since $\mathbf{E}_j$ depends on ensemble of induced dipoles, $\mathbf{p}_j$ and $\mathbf{E}_j$ are determined using an iterative procedure.

Results and discussion

For most AH/metal systems, AH thin film growth on low-index surfaces of metal crystals starts with (100)-terminated islands, which may have several different in-plane orientations and consist of a two atomic layer (2L)-thick wetting layer[9,11,63,64] [see Fig. 1(c)]. Moreover, a third atomic layer can grow on top of this wetting bilayer before the AH film fully covers the metal substrate.[9,64] Thus, already for deposited amounts of AH corresponding to less than two monolayers (2 ML), the AH film can feature some three atomic layer (3L)-thick domains [see Fig. 1(d)].

For KCl/Ag(100), the island growth mode and the (100) termination and in-plane orientation of the KCl islands have been confirmed by atomic-resolution scanning tunneling microscopy.[65] The presence of a 2L-thick wetting layer for ultrathin KCl films grown on Ag(100), as well as the additional contribution of 3L-thick KCl domains, is evidenced by our own HRPES and NIXSW data shown below. To begin with, we introduce a simplified analysis of the HRPES data, where we neglect the possible presence of 3L-thick KCl domains. Thus, we consider only two different atomic sites, corresponding to the first and second atomic layers of an ideal KCl bilayer, respectively. From NIXSW measurements, we determine the vertical atomic positions of the K^+ and Cl^- ions in the different layers of the KCl film. Using these vertical positions, we analytically simulate the core-level binding energy shifts and compare the different effects contributing to these shifts. Finally, we introduce in the model the presence of a third atomic layer of KCl. Assuming that this third atomic layer of KCl covers the wetting KCl bilayer only partially, we theoretically model the contribution of five different atomic sites, corresponding to the two atomic layers of 2L-thick KCl domains and the three atomic layers of 3L-thick KCl domains, which we believe is responsible for the experimentally observed lineshape asymmetry of the K and Cl HRPES peaks.

HRPES data analysis

Figure 2 shows the HRPES spectra of the $2p$ core levels of chlorine (Cl $2p$) and potassium (K $2p$) measured for two KCl films of different nominal thicknesses (i.e., 1 ML and 2 ML) grown on Ag(100). Taking into account the spin-orbit splitting of both Cl $2p$ and K $2p$ levels, all spectra in Fig. 2 can be fitted with four peaks representing two independent components of spin-orbit doublets, marked in red and blue. In the following, these two independent components are referred to as the lower binding energy (LBE) and the higher binding energy (HBE) components, respectively. In a simplified analysis, this observation indicates that two kinds of atomic sites coexist. Their different dielectric environments yield an energy-shifted replica of the doublet. In the Supplementary Information (see Fig. S1), we show that the energy position and lineshape of the Ag $3d$ core-level HRPES peaks are not modified or shifted when 1 or 2 ML of KCl is deposited on the Ag(100) surface, which indicates that KCl does not chemically react with Ag. Therefore, the electron binding energy shifts observed for Cl $2p$ and K $2p$ core levels are not due to K-Ag or Cl-Ag covalent bonding or alloying. Previously, the studies of the surface core-level shifts in bulk AH crystals reported HRPES spectra consisting of a superposition of a surface-ion and a bulk-ion contribution, shifted in energy with respect to each other.[42] Accordingly, we interpret the results shown in Fig. 2 as due to the contribution of the ions at the KCl/Ag and KCl/vacuum interfaces.

In order to quantitatively analyze the LBE and HBE contributions mentioned above, we fit the peaks of the HRPES spectra as follows. We consider two doublets shifted in energy with respect to each other. The $2p_{3/2}$ and $2p_{1/2}$ doublet is constrained to have a $2:1$ peak area ratio (based on the multiplicity of each spin state), equal FWHM for the two peaks of the doublet, and a peak separation of 1.63 eV for chlorine and 2.77 eV for potassium. The results of this fit are given in Table 1 and Table 2. Thus, we determine the energy shift between the LBE and HBE contributions in the $2p$ HRPES spectra, which is about 0.7 eV for chlorine at 1 ML (0.8 eV at 2 ML) and 0.9 eV for potassium (at 1 and 2 ML).

From the spectra shown in Fig. 2(a-d) and the peak area ratio given in Tab. 1, the height

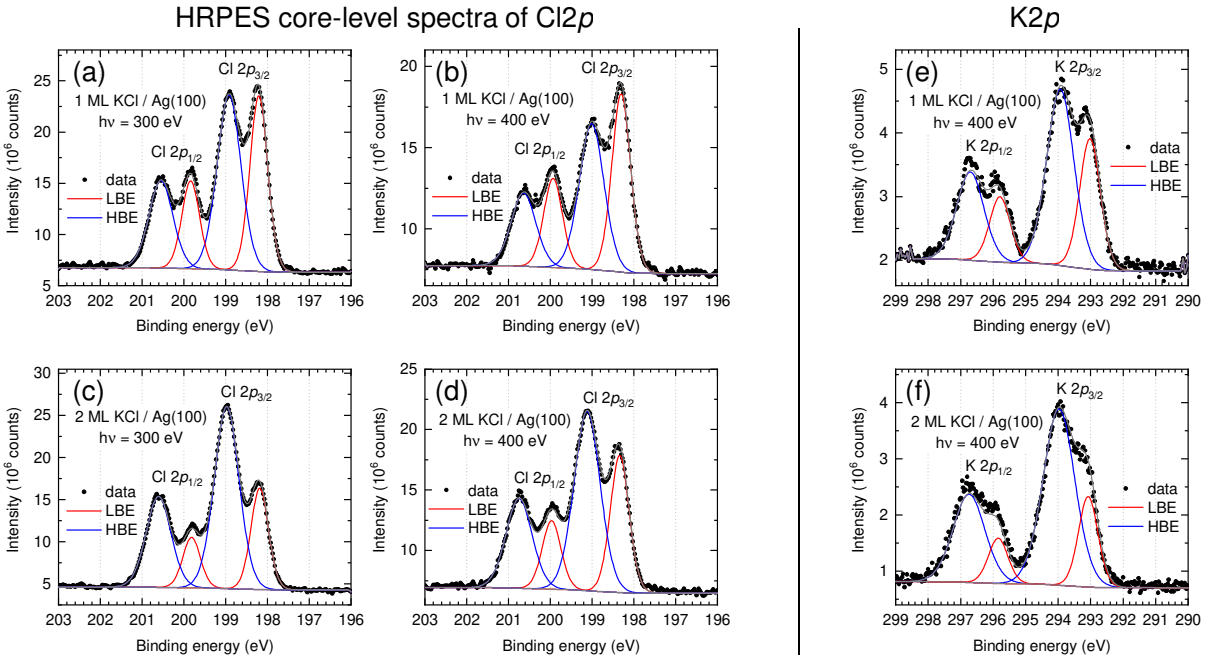

Figure 2: (a-d) Cl $2p$ and (e,f) K $2p$ HRPES spectra of two different ultrathin KCl films grown at room temperature on Ag(100). The photoemission intensity is plotted as a function of the electron binding energy. The nominal thickness of the two KCl films is 1 ML and 2 ML, respectively. The X-ray photon energy is indicated in the panels. The experimental data are fitted using two doublets of pseudo-Voigt functions, referred to as the lower binding energy (LBE, red line) and higher binding energy (HBE, blue line) components, over a Shirley baseline (bottom gray line). The top grey line is the envelope of the fit.

Table 1: Results of the peak-fitting analysis of the Cl $2p_{3/2}$ line from the HRPES spectra shown in Figs. 2(a) to 2(d). First column indicates the panel of Fig. 2 where the spectrum is shown. Second column is the nominal thickness of the KCl film, expressed in monolayers (ML). Third column refers to the used X-ray photon energy ($h\nu$). LBE and HBE stand for the lower and higher binding energy contributions discussed in the text. E is the binding energy position of the peak, as determined from the fit. ΔE corresponds to the shift between the energy positions of the LBE and HBE peaks. Last column gives the peak area ratio of the HBE versus the LBE contribution. All binding energies (E) are corrected for the Fermi level energy, which is determined experimentally for each film thickness and photon energy.

panel	thick. (ML)	$h\nu$ (eV)	Cl $2p_{3/2}$					
			LBE		HBE		ΔE (eV)	peak area ratio HBE/LBE
			E(eV)	FWHM(eV)	E(eV)	FWHM(eV)		
(a)	1	300	198.47	0.50	199.19	0.67	0.72	1.34
(b)	1	400	198.52	0.53	199.23	0.70	0.71	1.08
(c)	2	300	198.45	0.49	199.24	0.70	0.79	2.54
(d)	2	400	198.53	0.53	199.31	0.73	0.78	1.83

Table 2: Results of the peak-fitting analysis of the K $2p_{3/2}$ line from the HRPES spectra shown in Figs. 2(e) and 2(f). Same notation is used as in Tab. 1. The X-ray photon energy ($h\nu$) is 400 eV. All binding energies (E) are corrected for the Fermi level energy, which is determined experimentally for each film thickness and photon energy.

panel	thick. (ML)	K $2p_{3/2}$					
		LBE		HBE		ΔE	peak area ratio
		E(eV)	FWHM(eV)	E(eV)	FWHM(eV)	(eV)	HBE/LBE
(e)	1	293.29	0.75	294.20	0.99	0.91	1.77
(f)	2	293.34	0.71	294.23	1.15	0.90	3.18

of the LBE peak relative to that of the HBE peak is higher in the Cl $2p$ HRPES spectra measured at a photon energy of 400 eV than in the spectra measured at 300 eV. This is because the mean free path of the photoelectrons in the sample is dependent on their kinetic energy. The kinetic energy of the photoemitted electrons equals the difference between the energy of the absorbed photons and the binding energy of the electrons in the probed core level. Hence, for a given core level, the kinetic energy of the photoelectrons increases with the photon energy. In the considered kinetic energy range (i.e., about 100-200 eV), the mean free path of electrons in KCl increases with kinetic energy.[66] Thus, the relative increase of the LBE contribution with the photon energy confirms that the KCl film consists of at least two atomic planes and indicates that the LBE contribution is from the Cl anions pertaining to the deepest atomic plane (i.e., the KCl plane at the interface with Ag). This finding is true for both the 1 ML and 2 ML KCl films, which confirms their growth mode in the form of a bilayer. Note that, here, we neglect the effect of the photon energy dependence of the X-ray penetration depth in the sample, because the KCl film thickness is orders of magnitude lower than the X-ray penetration depth at the considered photon energies.[67]

We also observe that the nominal thickness of the KCl film, i.e., 1 ML or 2 ML, has an effect on the Cl $2p$ and K $2p$ HRPES spectra. For a given photon energy, the HBE/LBE peak height ratio and the HBE peak FWHM are larger at 2 ML than at 1 ML (see in Fig. 2 and in Tab. 1 and Tab. 2). If the KCl film were only composed of two atomic layers, increasing the nominal thickness from 1 ML to 2 ML would only increase the surface coverage of the

film (from 50% to 100%), which is not expected to change the HBE/LBE peak height ratio and the HBE peak FWHM. From these observations, we infer that the KCl film must also feature thicker (e.g., 3L-thick) KCl domains, whose relative contribution is higher at 2 ML than at 1 ML. This is consistent with the most commonly observed growth mode of AH thin films on metals[9,63,64] and is further corroborated by our NIXSW measurements discussed below. Thus, the HBE peak is not only the contribution of the second KCl atomic layer, but is a sum of at least two contributions from the atomic layers that are on top of the first atomic layer, which exhibit binding energies that are too close to be spectrally resolved in Fig. 2. Nevertheless, we will show that the lineshape of this "multiplet" can be explained using the model derived below, provided that the presence of a third KCl atomic layer is taken into account. In the next section, we determine the vertical atomic positions in the KCl film, which are used to model the core-level binding energy shifts for each of the KCl atomic layers.

Vertical atomic positions (NIXSW measurements)

The NIXSW technique exploits the fact that, when the photon energy is scanned across the Bragg energy, the photoelectron yield from an atom changes in a way that is related to its vertical position, due to the formation of X-ray standing waves. Hereby, the vertical position of the atom is defined as the distance from the extended Bragg planes of the substrate. In the present study, these planes are the (200) lattice planes of the Ag substrate, which are distant of $d_{(200)} = 2.04$ Å from each other. The photoemission spectra of a KCl thin film on Ag(100) shown in Figure 3 are recorded 10 eV below the Bragg energy, i.e., in the absence of X-ray standing waves. Despite the lower resolution (due to the higher photon energy used), the spectra shown in Fig. 3 exhibit the same splitting of the lines into two doublets (refered to as the LBE and HBE components) as the spectra shown in Fig. 2. In order to determine the vertical atomic positions, we measure the photoemission spectra at various photon energies around the Bragg energy. We fit the LBE and HBE components in these spectra as shown

in Fig. 3 and thus we obtain the curve of the photoemission yield as a function of the photon energy for each (LBE/HBE) component (see Fig. S2 in the Supplementary Information). This fitting analysis provides two parameters, i.e., the coherent fraction f_c and the coherent position p_c, which characterize the height distribution and the averaged vertical height of the respective atoms, respectively.[51] In Fig. 3(c), f_c and p_c are represented by a vector in the complex plane, i.e., the *Argand* vector $\mathbf{F} = f_c \cdot \exp(i\,2\,\pi\,p_c)$, where p_c and f_c correspond to the angle and length of the vector, respectively.

Figure 3(c) shows that, for a given (LBE or HBE) component of the spectra, the Argand vectors for the Cl^- and K^+ ions are comparatively close to each other. This implies similar coherent positions, i.e., similar vertical heights of the respective emitters. Hence, the Cl^- and K^+ ions responsible for each (LBE/HBE) component must pertain to the same atomic layer of the KCl film. In order to determine which of the two components corresponds to the top or bottom layer of the KCl film, we calculate the absolute heights d_c with respect to the outermost Ag(200) Bragg-plane. We use the relation $d_c = (n+p_c)\times 2.04$ Å, with appropriate integer values of n. The results are shown in Table 3. Note that the actual position of the topmost Ag layer may deviate from that of the Bragg plane due a possible relaxation, leading to a modified layer spacing between the topmost Ag layers. Nevertheless, our following argument remains valid, as we consider differences in height. A reasonable spacing Δd_c between the two layers is only obtained when the HBE and LBE components are assigned to the upper and lower layers, respectively. This requires values of $n = 3$ for the HBE and $n = 1$ for the LBE component. It yields a spacing $\Delta d_c = [(3+p_c^{\mathrm{HBE}})-(1+p_c^{\mathrm{LBE}})]\times 2.04$ Å$= 3.23$ Å for K^+ and 3.30 Å for Cl^-. These values are close to $d_{\mathrm{KCl(200)}} = 3.15$ Å, the distance between the atomic planes in bulk KCl. In the alternative case, if the components were assigned in the reverse order, values of Δd_c (e.g., for K^+, 4.93 Å or 2.89 Å) would be obtained, which deviate too much from $d_{\mathrm{KCl(200)}}$. Hence, from the vertical positions, we assign the HBE components to the ions at the KCl/vacuum interface, and the LBE components to the ions at the KCl/Ag interface. This assignment is in agreement with the photon-energy dependence of the HBE

and LBE components in the HRPES spectra, as discussed above.

For an ideal bilayer of KCl consisting of only two atomic layers, with the same number of ions in the upper and lower atomic layer, the Argand vector of the integrated intensity is expected to be located exactly at the middle of the line connecting the vectors of the HBE and LBE components (see. Fig. 3). (Here, we neglect the attenuation of the photoelectrons because the mean free path of electrons in KCl exceeds 500 Å at this photon energy.) However, Figure 3 shows that the Argand vector of the integrated intensity is shifted in the direction of the HBE component. We determine the molar fractions (denoted by [...]) according to the "lever rule" as [K-HBE]:[K-LBE]=1.14 and [Cl-HBE]:[Cl-LBE]=1.38. From these values we conclude that our film is not an ideal bilayer, but that an incomplete third layer with a relative coverage between 14 and 38% (deduced from the K2p and Cl2p data, respectively) contributes to the HBE component. The photoemission of this third layer contribution cannot be separated spectroscopically from that of the second layer. Its presence causes a small reduction of the coherent fraction of the HBE components. In addition, the height of the second layer is slightly underestimated by 0.02 Å. More details of the NIXSW analysis are given in the Supplementary Information.

In the next section, we use a simple analytical model and the vertical atomic positions determined here to calculate the theoretical binding energy shifts and we compare them to our experimental observations.

Analytical model

To model the core-level binding energy shifts in ultrathin KCl films on Ag(100), we use an electrostatic model, which is similar to the localized-hole, point-ion model previously employed by Citrin and Thomas[56] and by Mahan[57,68] to simulate the photoemission from bulk AH crystals. This model is based on the assumption that a modification of the coordination or dielectric environment of an ion shifts its core-level binding energies by a value that is independent of the considered electronic levels. In other words, the same energy shift must

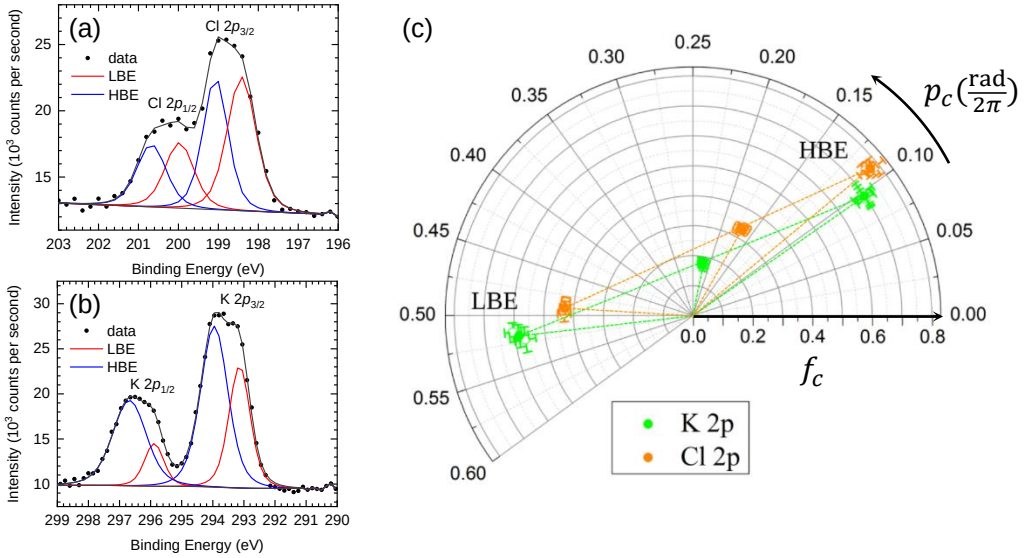

Figure 3: (a) Cl $2p$ and (b) K $2p$ X-ray photoemission spectra of the ultrathin KCl film used for the determination of the vertical atomic distances. The KCl film is grown at 200 K on Ag(100). The experimental data are fitted using two peak functions referred to as the lower binding energy (LBE, red line) and higher binding energy (HBE, blue line) components. The top and bottom grey lines are the baseline and the envelope of the fit, respectively. (c) Argand diagram of the K $2p$ and Cl $2p$ X-ray photoemission signals. The Argand vectors of the integrated intensities ($\diamond$) exhibit a small coherent fraction and are close to the origin. The Argand vectors of the HBE and LBE components are nearly on opposite sides of the origin. The Argand vectors of the integrated signal are linear combinations of the Argand vectors of the HBE and LBE components, as highlighted by the dashed lines. The diagram includes two independent data sets (open symbols) and the averaged data (solid symbols), which are all very close to each other.

Table 3: Coherent positions p_c and fractions f_c of an about two monolayer thick KCl(001) film on Ag(100). The vertical heights were calculated according to: $d_c = (n+p_c)\times 2.04$ Å with the given values of n. Typical error bars of the coherent fractions f_c and coherent positions p_c are ± 0.02 and ± 0.01, respectively. Error bars of the vertical heights d_c values range between ± 0.01 and ± 0.02 Å. The Δd_c value given for K $2p$ (for Cl $2p$) denotes the vertical height difference between the K^+ ions (Cl^- ions) in the top and bottom layers of the KCl film.

	signal	f_c	p_c	n	d_c (Å)	Δd_c (Å)
	LBE	0.59	0.51	1	3.09	
K 2p	HBE	0.68	0.095	3	6.32	3.23
	integral	0.18	0.22			
	LBE	0.45	0.50	1	3.06	
Cl 2p	HBE	0.79	0.12	3	6.36	3.30
	integral	0.33	0.17			

be observed for all the core levels of this ion. Thus, we calculate electronic energies and only consider their shifts as compared to the energies of a reference system, e.g., the bulk KCl crystal or the first atomic KCl layer at the KCl/Ag interface. We analytically calculate the energy shifts due to the dielectric screening and the electronic polarization effects, i.e., the Madelung term and the Mott-Littleton term. In these calculations, we include the substrate-induced image charge effects. Following Mahan,[57] we neglect the short-range repulsive forces.[56,68] We ignore the hole-phonon interactions, since these interactions are not expected to contribute significantly to the core-level binding energy shifts.[57] This said, the hole left in the ionic lattice in the final state of the photoemission process is expected to efficiently couple to the optical phonon excitations of the alkali halide. The hole-phonon coupling thus contributes to the broadening of the core levels similarly to the mechanism responsible for the Gaussian broadening of the vacancy states in ionic crystal films.[69]

As a preliminary test, we use this model to determine the surface core-level shifts Δ_s of a bulk KCl crystal. These are the shifts of the electron binding energy of the K^+ and Cl^- ions at the surface of a bulk KCl crystal, i.e., at the interface between KCl and the vacuum, relative to the K^+ and Cl^- ions inside the bulk crystal, respectively. We obtain $\Delta_s = -0.098$ eV ($\Delta_{Mad} = -0.306$ eV for the Madelung term alone) for surface Cl anions and 0.529 eV ($\Delta_{Mad} = 0.306$ eV) for surface K cations, in reasonable agreement with the values reported by Wertheim et al,[42] i.e., $\Delta_s \approx -0.11$ eV ($\Delta_{Mad} = -0.307$ eV) for Cl^- and $\Delta_s = 0.465 \pm 0.005$ eV ($\Delta_{Mad} = 0.307$ eV) for K^+. To apply this model to the KCl films on Ag, we use the vertical atomic distances measured by NIXSW to calculate the image charge effects due to the electric field screening by the metal, which depend on the distance between the ions in the film and the metal surface. (Here, the metal surface means the surface atomic plane of the Ag substrate. The rumpling is not accounted for.)

Two-layer model

The results of our calculations for a 2L-thick KCl wetting layer on Ag(100) are shown in Table 4. It contains the theoretical binding energy shifts with respect to the bulk ($\Delta_{/bulk}$) and with respect to the first KCl atomic layer at the KCl/Ag interface ($\Delta_{/1}$). In addition, the table indicates how much the modification of the Madelung potential contributes to the total binding energy shifts (see the Madelung term in the third and fourth column of Tab. 4 and the total binding energy shifts in the last two columns). In Tab. 4, the image charge effects are included in the calculations. For comparison purpose, the results of the calculations performed without taking into account the image charge effects are shown in Table 5. Note that all theoretical values are highly sensitive to the vertical positions of the ions; thus, the experimental uncertainties in the vertical heights determined from NIXSW measurements and used in the calculations may lead to larger uncertainties in the core-level energies than the precision of the theoretical values given in Tabs. 4 and 5.

Table 4: Theoretical core-level binding energy shifts calculated for a 2L-thick KCl film on Ag(100) with consideration of the image charge effects. $\Delta_{/bulk}$ and $\Delta_{/1}$ are the binding energy shifts relative to bulk KCl and to the first atomic layer of the KCl film, respectively. The 1^{st} and 2^{nd} atomic layers of the KCl film are the KCl layers at the KCl/Ag and KCl/vacuum interfaces, respectively. The values in bold characters in the last column are to be compared to the experimentally measured binding energy shifts, noted ΔE in Tabs. 1 and 2. See text for more details.

Ion	Atomic layer	Madelung		Madelung + Mott-Littleton	
		$\Delta_{/bulk}$(eV)	$\Delta_{/1}$(eV)	$\Delta_{/bulk}$(eV)	$\Delta_{/1}$(eV)
Cl^-	1^{st} (KCl/Ag)	-1.95	0	-1.03	0
	2^{nd} (KCl/vac.)	-0.95	1.00	-0.47	**0.56**
K^+	1^{st} (KCl/Ag)	-1.41	0	-0.38	0
	2^{nd} (KCl/vac.)	-0.25	1.16	0.24	**0.62**

As shown in Tab. 4, our model predicts core-level binding energy shifts of 0.56 eV for Cl^- and 0.62 eV for K^+, between the second and first atomic layers of a 2L-thick KCl film on Ag(100), which is in reasonable agreement with the experiment. Indeed, these theoretical

Table 5: Theoretical core-level binding energy shifts calculated for a 2L-thick KCl film on Ag(100), without taking into account the image charge effects. Same notations as in Tab. 4. See text for more details.

Ion	Atomic layer	Madelung		Madelung + Mott-Littleton	
		$\Delta_{/bulk}$(eV)	$\Delta_{/1}$(eV)	$\Delta_{/bulk}$(eV)	$\Delta_{/1}$(eV)
Cl^-	1^{st} (KCl/Ag)	-0.18	0	0.25	0
	2^{nd} (KCl/vac.)	-0.23	-0.047	0.20	**-0.047**
K^+	1^{st} (KCl/Ag)	0.52	0	0.97	0
	2^{nd} (KCl/vac.)	0.48	-0.046	0.92	**-0.047**

values match to 0.15 - 0.29 eV (i.e., to 21 - 32%) the values obtained from the simple peak fitting analysis shown in Fig. 2, i.e., 0.71 - 0.79 eV for Cl $2p$ and 0.90 - 0.91 eV for K $2p$ HRPES peaks. From Tabs. 4 and 5, we also infer that such a semi-quantitative match between this simple analytical model and the experiment is only obtained when both the polarization effects and the metal substrate screening effects (modeled using the image-charge approximation) are taken into account. Indeed, omitting these effects leads to calculated binding energy shifts that differ by 0.7 to 0.9 eV from the experimental data.

With the polarization and image-charge effects properly included in the model, the remaining discrepancies between the simulated and experimental data may be due to uncertainty on the vertical positions of the ions used in the model, which are inferred from NIXSW measurements. Figure 4 shows the effect of varying the vertical positions of the Cl^- and K^+ ions of the first atomic layer (at the KCl/Ag interface) on the calculated binding energy shifts relative to the first atomic layer, i.e., the values of $\Delta_{/1}$ in bold characters in Tab. 4. Here, the vertical positions of the Cl^- and K^+ ions of the second atomic layer (at the KCl/vacuum interface) are kept constant. Similar results are obtained when the vertical positions of the Cl^- and K^+ ions of the second atomic layer are also changed and the vertical distances between the ions of the two atomic layers are kept constant (see Fig. S3 in the Suppementary Information), which highlights the dominating effect of the vertical positions of the ions at the KCl/Ag interface. The crosses at the center of the graphs shown in Fig. 4 indicate the vertical positions used in the calculations shown in Tabs. 4 and 5 and

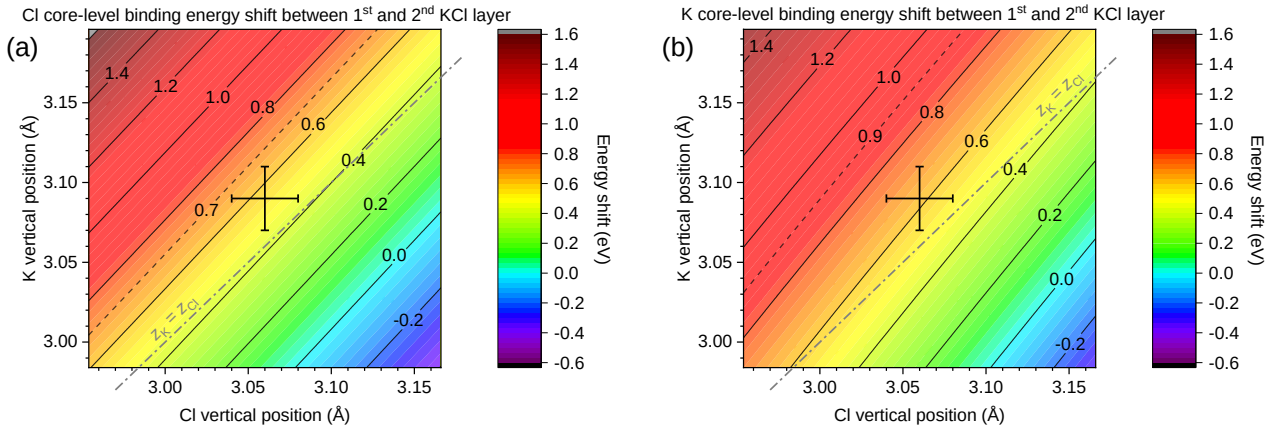

Figure 4: Theoretical core-level binding energy shifts calculated for a 2L-thick KCl film on Ag(100) with consideration of the image charge effects. The binding energy shifts relative to the first atomic layer of the KCl film (refered to as $\Delta_{/1}$ in Tab. 4) is plotted as a function of the vertical distance of the Cl^- and K^+ ions of the first atomic layer from the surface atomic plane (see z' in Fig. 1(b)). The vertical positions of the ions in the second atomic layer are kept constant. The first and second atomic layers of the KCl film are the KCl layers at the KCl/Ag and KCl/vacuum interfaces, respectively. The crosses at the center of the graphs indicate the vertical positions (d_c) deduced from the NIXSW measurements and used in the calculations shown in Tabs. 4 and 5. The horizontal and vertical widths of the cross correspond to the estimated maximal uncertainty on d_c, i.e., ± 0.02 Å.

the estimated maximal uncertainty on these positions, which equals ±0.02 Å. Using these error bars, we graphically evaluate the resulting uncertainty range of the calculated binding energy shifts. We find $\Delta_{/1} = 0.56 \pm 0.18$ eV for Cl^- and $\Delta_{/1} = 0.62 \pm 0.16$ eV for K^+. Thus, the experimental value of this energy shift, inferred from the analysis of the HRPES spectra (see ΔE in Tabs. 1 and 2), is within the uncertainty range of the theoretical value for Cl^-, with $\Delta E = 0.71 - 0.72$ eV at 1 ML, but remains underestimated by the model for K^+, with $\Delta E = 0.91$ eV at 1 ML.

Three-layer model

Additional discrepancies between the simulated and experimental data may result from the fact that we assume in the simulations an ideal 2L-thick KCl film on Ag. In fact, we omit the presence of thicker (e.g., 3L-thick) KCl domains. As well, we neglect the multiplet character of the HBE contribution in the simplified peak fitting analysis shown in Fig. 2. In order to describe this multiplet character, we use the model introduced above to calculate the core-level binding energy shifts expected for a 3L-thick KCl film on Ag(100). In the absence of accurate NIXSW data for the third KCl layer, we assume that the anions and cations in the third KCl layer are located in the same horizontal plane, whose vertical distance from the average plane of the second KCl layer is taken as that of the bulk KCl crystal (i.e., 3.15 Å), as shown in Fig. 1(b). Table 6 contains the results of these calculations. In the same way as in Tab. 4, we indicate the theoretical binding energy shifts with respect to the bulk ($\Delta_{/bulk}$) and with respect to the first KCl atomic layer of a 2L-thick KCl film on Ag ($\Delta_{/1}$). To stress the importance of the different contributions, we also show the results obtained neglecting the polarization of the KCl layer, i.e., assuming only the point charge contribution (the Madelung term). In Tab. 6, the substrate-induced image charge effects are included in all the calculations.

As shown in the last column of Tab. 6, adding a third KCl atomic layer in the model reduces the theoretical core-level binding energy of the Cl^- and K^+ ions at the KCl/Ag

Table 6: Theoretical core-level binding energy shifts calculated for a 3L-thick KCl film on Ag(100). $\Delta_{/bulk}$ and $\Delta_{/1}$ are the binding energy shifts relative to bulk KCl and to the first atomic layer of a 2L-thick KCl film on Ag(100), respectively. The 1^{st} and 3^{rd} atomic layers of the KCl film are the KCl layers at the KCl/Ag and KCl/vacuum interfaces, respectively. See text for more details.

Ion	Atomic layer	Madelung		Madelung + Mott-Littleton	
		$\Delta_{/bulk}$(eV)	$\Delta_{/1}$(eV)	$\Delta_{/bulk}$(eV)	$\Delta_{/1}$(eV)
Cl^-	1^{st} (KCl/Ag)	-1.95	-0.003	-1.04	**-0.017**
	2^{nd} (KCl/KCl)	-0.63	1.32	-0.33	**0.70**
	3^{rd} (KCl/vac.)	-0.82	1.13	-0.48	**0.54**
K^+	1^{st} (KCl/Ag)	-1.41	0.003	-0.40	**-0.012**
	2^{nd} (KCl/KCl)	-0.54	0.87	-0.24	**0.15**
	3^{rd} (KCl/vac.)	-0.21	1.20	0.14	**0.52**

interface by less than 0.02 eV. The theoretical core-level binding energy of the ions at the KCl/vacuum interface of the 3L-thick KCl film is 0.02 eV-lower for Cl^- and 0.10 eV-lower for K^+, as compared to the 2L-thick KCl film. In fact, the most striking difference between the results shown in the last columns of Tabs. 4 and 6 concerns the ions in the second layer of the thickest film, which are neither at the interface with the substrate nor with the vacuum. Adding an extra layer to the double-layer film changes the environment of these ions and leads to the change of their core-level binding energy primarily because of the change of the Madelung potential.

Overall, our results help understand the dissimilar lineshapes of the LBE and HBE peaks shown in Fig. 2. A realistic description of an ultrathin KCl film grown on Ag(100) must take into account the presence of 2L and 3L-thick KCl domains. Thus, the theoretical core-level binding energy shifts calculated for both KCl film thicknesses should be observed in the HRPES spectra. According to Tabs. 4 and 6, the LBE component in Fig. 2 must be the superposition of two peaks, due to the ions at the KCl/Ag interface of the 2L and 3L-thick KCl domains, whose energy shift relative to each other (i.e., less than 0.02 eV) is small compared to their FWHM (about 0.5 eV for Cl^- and 0.7 eV for K^+). The photoemission peaks from the other ions, i.e., those in the second and third layers of the KCl film, must

contribute to the HBE component, to the exception of the peak shifted by 0.15 eV in the last column of Tab. 6 for K^+, which lies at an energy position close to the LBE component. Because these peaks are shifted with respect to each other by amounts of energy that are not negligible compared to their FWHM, the resulting HBE component features a larger FWHM (by about 30 to 40% for Cl^- and 30 to 60% for K^+, according to Tabs. 1 and 2) and a more dissymmetric lineshape, as compared to the LBE component in Fig. 2.

Table 7: Theoretical core-level binding energy shifts calculated for a 3L-thick KCl film on Ag(100), without taking into account the image charge effects. Same notations as in Tab. 6. See text for more details.

Ion	Atomic layer	Madelung		Madelung + Mott-Littleton	
		$\Delta_{/bulk}$(eV)	$\Delta_{/1}$(eV)	$\Delta_{/bulk}$(eV)	$\Delta_{/1}$(eV)
Cl^-	1^{st} (KCl/Ag)	-0.18	-0.003	-1.19	**-0.08**
	2^{nd} (KCl/KCl)	0.09	0.27	-1.09	**0.03**
	3^{rd} (KCl/vac.)	-0.36	-0.18	-1.39	**-0.27**
K^+	1^{st} (KCl/Ag)	0.53	0.003	-0.85	**-0.07**
	2^{nd} (KCl/KCl)	0.18	-0.34	-1.37	**-0.59**
	3^{rd} (KCl/vac.)	0.26	-0.27	-1.15	**-0.38**

For comparison purpose, the results of the calculations performed without taking into account the metal substrate screening effects (i.e., the image charge effects) are shown in Table 7. When the image charges are not taken into account, the core-level binding energy shifts calculated for the first and third KCl atomic layers differ by -0.19 eV for Cl^- and -0.31 eV for K^+ (see last column in Tab. 7), whereas they differ by $+0.56$ eV for Cl^- and $+0.53$ eV for K^+ when the image charges are taken into account in the calculations (see last column in Tab. 6). Thus, the omission of electrostatic screening by the metallic substrate in the model can lead to errors in both the magnitude and the sign of the simulated binding energy shifts and, therefore, can lead to misidentification of contributions to the experimental photoemission spectra. This is because the image charge effects depend on the distance of the ions from the metal substrate as $\mathcal{U}_{ind} \approx \dfrac{q^2}{4z\epsilon_\infty}$ in atomic units, where $q = 1$ (a.u.) is the hole charge, z is the hole distance from the image plane of the metal, and ϵ_∞ is the electronic part of the dielectric constant of the ionic crystal. The role of the metal substrate leading

to the screening of the potential (image charge effect) is illustrated in Figure 5.

The image charge contribution

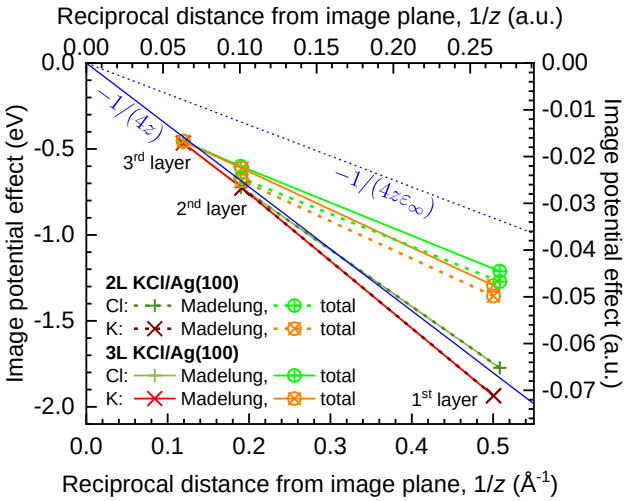

Figure 5: Contribution of the image charge effects to the modification of the Madelung potential and to the total binding energy shift (including the Madelung and Mott-Littleton terms) as a function of the reciprocal distance ($1/z$) of the ions from the image plane of the Ag(100) surface. The solid and dotted blue lines are the plot of the functions $-1/(4z)$ and $-1/(4z\epsilon_\infty)$, where energy and distance are expressed in atomic units (a.u.). These two functions correspond to the classical unscreened and screened image potential, respectively. Here, screening is due to the electronic part of the dielectric constant and we use the approximation $\epsilon_\infty = 2$.

In Fig. 5, the contribution of the image charge effects to the modification of the Madelung potential and to the total binding energy shift is plotted as a function of the reciprocal distance of the ions from the image plane of the Ag(100) surface. (This image plane is about 1.09 Å beyond the surface atomic plane of the metal in the vacuum region.[61]) The contribution of the image charge effects corresponds to the energy difference between the electron binding energies calculated with and without including the image charges, respectively. When only the Madelung potential is considered, no hole screening by the KCl crystal is acting and the image charge contribution can be well described by the classical image potential $\mathcal{U} = -1/(4z)$, where z is the distance from the image plane, and energy ($\mathcal{U}$) and distance (z) are expressed in atomic units (a.u.). When the electronic polarization effects (i.e., the Mott-

Littleton term) are added, the total image charge contribution is comparatively smaller and its distance dependence is well described by the function $\mathcal{U} = -1/(4z\epsilon_\infty)$, i.e., the classical image potential screened by the electronic part of the dielectric constant ϵ_∞, where we use the approximation $\epsilon_\infty = 2$.

General discussion

Before closing, we discuss the strengths and weaknesses of the theoretical approach described above. The simple analytical model used provides a semi-quantitative understanding of the HRPES measurements shown in Fig. 2. It indicates that at least five doublets corresponding to different atomic layers of the KCl film are present, which merge into two groups of peaks (i.e., the LBE and HBE contributions in Fig. 2) that are not spectrally resolved, because the peak energy shifts relative to each other are too small as compared to their FWHM. The shifts calculated from the model help explain the dissimilar FWHM and lineshapes of the LBE and HBE contributions. Moreover, our calculations reveal that the modification of the Madelung potential, the polarization of the neighboring ions and the substrate-induced image charges contribute to the core-level binding energy shifts by amounts of energy that are of the same order of magnitude and that, thus, none of these can be neglected. Nevertheless, the model used is based on several simplifications. Because the hole-phonon interactions are not treated, the lineshape of the different contributions is not known and the choice of the fitting peak function is based on simple assumptions. Furthermore, other existing atomic sites in ultrathin AH films, e.g., ions at the island edges, and possible atomic relaxation in the KCl adlayers, which may yield additional contributions with different binding energy shifts, are not considered in the present model. Further calculations may also be required to estimate the error due to the neglect of the change of the short-range ion-ion repulsion between K^+ (Cl^-) ion and its Cl^- (K^+) neighbours upon creation of the hole at the inner shell of this ion. Nevertheless, we expect short-range repulsion effects to be similar in the different atomic layers of the KCl film and, therefore, not to significantly contribute to the core-level binding

energy shifts in one layer as compared to the other layers of the KCl film. Last but not least, our results highlight the strong dependence of the calculated core-level binding energy shifts on the vertical ion positions used in the model. In particular, modifying the height difference between the K^+ and Cl^- ions, i.e., the intralayer corrugation (or "rumpling") of the first atomic layer of the KCl film (at the KCl/Ag interface) has the strongest effect. On the other hand, varying both ion positions by the same amount yields negligible modification of the core-level binding energy shifts. Note that varying the vertical positions of the K^+ and Cl^- ions by the same amount is equivalent to changing the distance of the image plane from the surface atomic plane of Ag(100), while keeping the ions at their initial positions.

More generally, AH thin films on metal crystals are increasingly used in surface science and nanophysics experiments, especially as substrates for spectroscopy and microscopy techniques based on charge particles and/or scanning probes, to control the properties of individual atoms and molecules. In this context, our results may help understand the effects of the interaction of the AH ions with their dielectric environment and with the metallic substrate. Understanding these effects is key to correctly interpret the results of experimental measurements and control the properties of the adsorbed atoms or molecules. We anticipate that further experiments on other metal-supported ultrathin AH films and in conditions yielding higher energy resolution (e.g., at lower sample-cooling temperature) may help validate our simple model. As well, future refinement of our theoretical approach may allow to predict the lineshape of the HRPES peaks and eventually extract from peak fitting analysis the statistical distribution of atomic sites.

Conclusion

In this work, we have experimentally and theoretically investigated the core-level binding energy shifts in ultrathin KCl films, 1 and 2 ML in nominal thickness, grown on Ag(100). Based on HRPES and NIXSW measurements, we showed that the Cl^- anions and K^+ cations

of the first atomic layer of KCl/Ag(100) exhibit lower $2p$ core level energies as compared to the ions of the second atomic layer. The corresponding photoemission peaks are separated in energy by about 0.7 eV for Cl^- at 1 ML (0.8 eV at 2 ML) and 0.9 eV for K^+ (at 1 and 2 ML). Thus, the peak doublet that is expected for $2p$ core-level photoemission peaks due to spin-orbit coupling is further duplicated, depending on whether the electrons are emitted from ions at the KCl/Ag or KCl/vacuum interface. We have demonstrated that the simple lineshapes known for bulk materials transform into intricated multiplets for ultrathin films, due to the different dielectric environment of the atoms in each atomic plane of the films. To clarify the composition of these multiplets, we derived a simple model, which includes the modification of the Madelung potential, the polarization of the neighboring ions, and the substrate-induced screening modeled using the image-charge approximation. Thus, we showed that the doublet observed at the lowest binding energy in HRPES mainly results from the merging of two contributions, i.e., from the ions at the KCl/Ag interface in the two (2L) and three atomic layer (3L)-thick domains, with (only for K^+) an additional contribution from the (K^+) ions in the second layer of the 3L-thick KCl domains. The doublet found at the highest binding energy consists of three contributions for Cl^-, and two for K^+, which we assigned to the ions at the KCl/vacuum interfaces and (only for Cl^-) the (Cl^-) ions in the second layer of the 3L-thick KCl domains. We have demonstrated that both the polarization and image charge effects are crucial to obtain semi-quantitative predictions of the core-level binding energy shifts, given that omitting these effects leads to errors in their estimation by as much as 0.9 eV (see K^+ in the last column of Tabs. 6 and 7). Finally, we have highlighted the crucial effect of the intralayer corrugation of the first atomic layer of the KCl film (at the KCl/Ag interface) on the calculated binding energy shifts.

Acknowledgement

Experimental support by Timo Heepenstrick is acknowledged. We thank Diamond Light Source for access to beamline I09 (under proposal SI14878) that contributed to the results presented here and the team of the beamline I09, D. Duncan, P. Kumar, and T.-L. Lee. Financial support by the DFG under Project No. So407/6-3 and SFB 1083 is acknowledged. This work is supported by public grants from the Agence Nationale de la Recherche (ANR) under Contract No. ANR-16-CE24-0003 (M-Exc-ICO) and from the LabEx PALM overseen by the Agence Nationale de la Recherche (ANR) as part of the "Investissements d'Avenir" program (Contract No. ANR-10-LABX-0039).

Supporting Information Available

The following files are available free of charge.

- suppinfo.pdf: HRPES spectra of the Ag $3d$ core-level doublet for KCl films grown on Ag(100) and for clean Ag(100), which show the absence of any significant X-ray beam induced degradation of the KCl films and the absence of K-Ag or Cl-Ag covalent bonding or alloying; HRPES spectrum measured in the binding energy region of the C $1s$ core-level singlet showing the absence of any significant carbon contamination in the sample; X-ray photoemission (XPS) survey spectra of KCl films grown on Ag(100) confirming the absence of any significant contamination of the sample and of the preparations used in this study; the XPS spectra of the ultrathin KCl film used for the determination of the vertical atomic distances; additional information about the NIXSW measurements; photoelectron yield curves and reflectivity curves from NIXSW measurements.

References

(1) Kiguchi, M.; Inoue, H.; Saiki, K.; Sasaki, T.; Iwasawa, Y.; Koma, A. Electronic structure of alkali halide-metal interface: LiCl(001)/Cu(001). *Surf. Sci.* **2003**, *522*, 84–89.

(2) Repp, J.; Meyer, G.; Paavilainen, S.; Olsson, F. E.; Persson, M. Imaging Bond Formation Between a Gold Atom and Pentacene on an Insulating Surface. *Science* **2006**, *312*, 1196–1199.

(3) Bennewitz, R.; Barwich, V.; Bammerlin, M.; Loppacher, C.; Guggisberg, M.; Baratoff, A.; Meyer, E.; GÃijntherodt, H.-J. Ultrathin films of NaCl on Cu(111): a LEED and dynamic force microscopy study. *Surf. Sci.* **1999**, *438*, 289–296.

(4) Tegenkamp, C.; Pfnür, H.; Ernst, W.; Malaske, U.; Wollschläger, J.; Peterka, D.; Schröder, K. M.; Zielasek, V.; Henzler, M. Defects in epitaxial insulating thin films. *J. Phys.: Condens. Matter* **1999**, *11*, 9943–9954.

(5) Hebenstreit, W.; Redinger, J.; Horozova, Z.; Schmid, M.; Podloucky, R.; Varga, P. Atomic resolution by STM on ultra-thin films of alkali halides: experiment and local density calculations. *Surf. Sci.* **1999**, *424*, L321–L328.

(6) Kiguchi, M.; Entani, S.; Saiki, K.; Inoue, H.; Koma, A. Two types of epitaxial orientations for the growth of alkali halide on fcc metal substrates. *Phys. Rev. B* **2002**, *66*, 155424.

(7) Loppacher, C.; Zerweck, U.; Eng, L. M. Kelvin probe force microscopy of alkali chloride thin films on Au(111). *Nanotechnology* **2003**, *15*, S9–S13.

(8) Kikas, A.; Kisand, V.; Käämbre, T.; Ruus, R.; Nõmmiste, E.; Hirsimäki, M.; Valden, M.; Kukk, E.; Aksela, H.; Aksela, S. Insulating properties of ultrathin KF layers on Cu(100): Resonant Auger spectroscopy. *Surf. Sci.* **2005**, *584*, 49–54, Selected papers of the Fifth Nordic Conference on Surface Science (NCSS-5).

(9) Pivetta, M.; Patthey, F.; Stengel, M.; Baldereschi, A.; Schneider, W.-D. Local work function Moiré pattern on ultrathin ionic films: NaCl on Ag(100). *Phys. Rev. B* **2005**, *72*, 115404.

(10) Bennewitz, R. Structured surfaces of wide band gap insulators as templates for overgrowth of adsorbates. *J. Phys.: Condens. Matter* **2006**, *18*, R417–R435.

(11) Cabailh, G.; Henry, C. R.; Barth, C. Thin NaCl films on silver (001): island growth and work function. *New J. Phys.* **2012**, *14*, 103037.

(12) Bretel, R.; Le Moal, S.; Oughaddou, H.; Le Moal, E. Hydrogen-bonded one-dimensional molecular chains on ultrathin insulating films: Quinacridone on KCl/Cu(111). *Phys. Rev. B* **2023**, *108*, 125423.

(13) Barjenbruch, U.; Fölsch, S.; Henzler, M. Surface states on epitaxial thin films of NaCl and KCl. *Surf. Sci.* **1989**, *211-212*, 749–758.

(14) Fölsch, S.; Barjenbruch, U.; Henzler, M. Atomically thin epitaxial films of NaCl on germanium. *Thin Solid Films* **1989**, *172*, 123–132.

(15) Zielasek, V.; Hildebrandt, T.; Henzler, M. Surface color centers on epitaxial NaCl films. *Phys. Rev. B* **2000**, *62*, 2912–2919.

(16) Kolodziej, J.; Such, B.; Czuba, P.; Krok, F.; Piatkowski, P.; Szymonski, M. Scanning-tunneling/atomic-force microscopy study of the growth of KBr films on InSb(001). *Surf. Sci.* **2002**, *506*, 12–22.

(17) Krok, F.; Kolodziej, J.; Such, B.; Czuba, P.; Struski, P.; Piatkowski, P.; Szymonski, M. Dynamic force microscopy and Kelvin probe force microscopy of KBr film on InSb(001) surface at submonolayer coverage. *Surf. Sci.* **2004**, *566-568*, 63–67, Proceedings of the 22nd European Conference on Surface Science.

(18) Beinik, I.; Barth, C.; Hanbücken, M.; Masson, L. KCl ultra-thin films with polar and non-polar surfaces grown on Si(111)7 × 7. *Sci. Rep.* **2015**, *5*, 8223.

(19) Repp, J.; Meyer, G.; Stojković, S. M.; Gourdon, A.; Joachim, C. Molecules on Insulating Films: Scanning-Tunneling Microscopy Imaging of Individual Molecular Orbitals. *Phys. Rev. Lett.* **2005**, *94*, 026803.

(20) Steurer, W.; Repp, J.; Gross, L.; Scivetti, I.; Persson, M.; Meyer, G. Manipulation of the Charge State of Single Au Atoms on Insulating Multilayer Films. *Phys. Rev. Lett.* **2015**, *114*, 036801.

(21) Imada, H.; Miwa, K.; Imai-Imada, M.; Kawahara, S.; Kimura, K.; Kim, Y. Real-Space Investigation of Energy Transfer in Heterogeneous Molecular Dimers. *Nature* **2016**, *538*, 364.

(22) Zhang, Y.; Luo, Y.; Zhang, Y.; Yu, Y.-J.; Kuang, Y.-M.; Zhang, L.; Meng, Q.-S.; Luo, Y.; Yang, J.-L.; Dong, Z.-C. et al. Visualizing Coherent Intermolecular Dipole-Dipole Coupling in Real Space. *Nature* **2016**, *531*, 623.

(23) Doppagne, B.; Chong, M. C.; Lorchat, E.; Berciaud, S.; Romeo, M.; Bulou, H.; Boeglin, A.; Scheurer, F.; Schull, G. Vibronic Spectroscopy with Submolecular Resolution from STM-Induced Electroluminescence. *Phys. Rev. Lett.* **2017**, *118*, 127401.

(24) Doppagne, B.; Chong, M. C.; Bulou, H.; Boeglin, A.; Scheurer, F.; Schull, G. Electrofluorochromism at the single-molecule level. *Science* **2018**, *361*, 251–255.

(25) Yang, B.; Chen, G.; Ghafoor, A.; Zhang, Y.; Zhang, Y.; Zhang, Y.; Luo, Y.; Yang, J.; Sandoghdar, V.; Aizpurua, J. et al. Sub-nanometre resolution in single-molecule photoluminescence imaging. *Nat. Photonics* **2020**, *14*, 693–699.

(26) Imada, H.; Imai-Imada, M.; Miwa, K.; Yamane, H.; Iwasa, T.; Tanaka, Y.; Toriumi, N.;

Kimura, K.; Yokoshi, N.; Muranaka, A. et al. Single-molecule laser nanospectroscopy with micro-electron volt energy resolution. *Science* **2021**, *373*, 95–98.

(27) Vasilev, K.; Doppagne, B.; Neuman, T.; Rosławska, A.; Bulou, H.; Boeglin, A.; Scheurer, F.; Schull, G. Internal Stark effect of single-molecule fluorescence. *Nat. Commun.* **2022**, *13*, 677.

(28) Jiang, S.; Neuman, T.; Bretel, R.; Boeglin, A.; Scheurer, F.; Le Moal, E.; Schull, G. Many-Body Description of STM-Induced Fluorescence of Charged Molecules. *Phys. Rev. Lett.* **2023**, *130*, 126202.

(29) Hung, L. S.; Tang, C. W.; Mason, M. G. Enhanced electron injection in organic electroluminescence devices using an Al/LiF electrode. *Appl. Phys. Lett.* **1997**, *70*, 152–154.

(30) Hung, L. S.; Zhang, R. Q.; He, P.; Mason, G. Contact formation of LiF/Al cathodes in Alq-based organic light-emitting diodes. *J. Phys. D: Appl. Phys.* **2001**, *35*, 103–107.

(31) Brabec, C. J.; Shaheen, S. E.; Winder, C.; Sariciftci, N. S.; Denk, P. Effect of LiF/metal electrodes on the performance of plastic solar cells. *Appl. Phys. Lett.* **2002**, *80*, 1288–1290.

(32) Brown, T. M.; Friend, R. H.; Millard, I. S.; Lacey, D. J.; Butler, T.; Burroughes, J. H.; Cacialli, F. Electronic line-up in light-emitting diodes with alkali-halide/metal cathodes. *J. Appl. Phys.* **2003**, *93*, 6159–6172.

(33) Ma, L.; Yang, Y. Unique architecture and concept for high-performance organic transistors. *Appl. Phys. Lett.* **2004**, *85*, 5084–5086.

(34) Wang, S.; Chan, P. K. L.; Wah Leung, C.; Zhao, X. Controlled performance of an organic transistor memory device with an ultrathin LiF blocking layer. *RSC Adv.* **2012**, *2*, 9100–9105.

(35) Wang, H.; Amsalem, P.; Heimel, G.; Salzmann, I.; Koch, N.; Oehzelt, M. Band-Bending in Organic Semiconductors: the Role of Alkali-Halide Interlayers. *Adv. Mater.* **2014**, *26*, 925–930.

(36) Wan, S.; Zhang, G.; Niederhausen, J.; Wu, D.; Wang, Q.; Sun, B.; Song, T.; Duhm, S. Schottky contact formation by an insulator: Lithium fluoride on silicon. *Appl. Phys. Lett.* **2021**, *118*, 241601.

(37) Smith, J. R.; Arlinghaus, F. J.; Gay, J. G. Core-electron binding-energy shifts at surfaces. *Phys. Rev. B* **1982**, *26*, 1071–1074.

(38) Egelhoff, W. Core-level binding-energy shifts at surfaces and in solids. *Surf. Sci. Rep.* **1987**, *6*, 253–415.

(39) Riffe, D. M.; Wertheim, G. K.; Buchanan, D. N. E.; Citrin, P. H. Thermal and surface core-electron binding-energy shifts in metals. *Phys. Rev. B* **1992**, *45*, 6216–6225.

(40) Nelin, C. J.; Uhl, F.; Staemmler, V.; Bagus, P. S.; Fujimori, Y.; Sterrer, M.; Kuhlenbeck, H.; Freund, H.-J. Surface core-level binding energy shifts for MgO(100). *Phys. Chem. Chem. Phys.* **2014**, *16*, 21953–21956.

(41) Bagus, P. S.; Nelin, C. J.; Zhao, X.; Levchenko, S. V.; Davis, E.; Weng, X.; Späth, F.; Papp, C.; Kuhlenbeck, H.; Freund, H.-J. Revisiting surface core-level shifts for ionic compounds. *Phys. Rev. B* **2019**, *100*, 115419.

(42) Wertheim, G.; Buchanan, D.; Rowe, J.; Citrin, P. Surface-ion core-level shifts in alkali halides. *Surf. Sci.* **1994**, *319*, L41–L46.

(43) Patanen, M.; Bancroft, G. M.; Aksela, S.; Aksela, H. Direct experimental determination of the K 2*p* and Cl 2*p* core-level binding energy shifts between molecular and solid KCl: Line broadening effects. *Phys. Rev. B* **2012**, *85*, 125419.

(44) Kisand, V.; Kikas, A.; Kukk, E.; Nõmmiste, E.; Kooser, K.; Käämbre, T.; Ruus, R.; Valden, M.; Hirsimäki, M.; Jussila, P. et al. Substrate-induced effects in the creation and decay of potassium 2p core excitations in ultrathin films of KCl on copper. *J. Phys.: Condens. Matter* **2008**, *20*, 145206.

(45) Wang, H.; Oehzelt, M.; Winkler, S.; Ovsyannikov, R.; Koch, N.; Amsalem, P. Electronic properties and degradation upon VUV irradiation of sodium chloride on Ag(111) studied by photoelectron spectroscopy. *Electronic Structure* **2021**, *3*, 034008.

(46) Neaton, J. B.; Hybertsen, M. S.; Louie, S. G. Renormalization of Molecular Electronic Levels at Metal-Molecule Interfaces. *Phys. Rev. Lett.* **2006**, *97*, 216405.

(47) Zhao, J.; Pontius, N.; Winkelmann, A.; Sametoglu, V.; Kubo, A.; Borisov, A. G.; Sánchez-Portal, D.; Silkin, V. M.; Chulkov, E. V.; Echenique, P. M. et al. Electronic potential of a chemisorption interface. *Phys. Rev. B* **2008**, *78*, 085419.

(48) Soubatch, S.; Weiss, C.; Temirov, R.; Tautz, F. S. Site-Specific Polarization Screening in Organic Thin Films. *Phys. Rev. Lett.* **2009**, *102*, 177405.

(49) Zojer, E.; Taucher, T. C.; Hofmann, O. T. The Impact of Dipolar Layers on the Electronic Properties of Organic/Inorganic Hybrid Interfaces. *Adv. Mater. Interfaces* **2019**, *6*, 1900581.

(50) Barreto, J.; Caetano, R.; Ramos, M. I.; Alí, A.; Félix, G.; Annese, E.; Nilius, N.; Freund, H.-J.; Archanjo, B. S.; Achete, C. A. et al. Core-level binding energy shifts between interior, terrace and edge atoms in MnO(001) thin films. *Surf. Sci.* **2022**, *725*, 122159.

(51) Zegenhagen, J.; Kazimirov, A. *The X-Ray Standing Wave Technique - Principles and Applications*; Series on Synchrotron Radiation Techniques and Applications; World Scientific, 2013; Vol. 7.

(52) Polack, F.; Silly, M.; Chauvet, C.; Lagarde, B.; Bergeard, N.; Izquierdo, M.; Chubar, O.; Krizmancic, D.; Ribbens, M.; Duval, J. et al. TEMPO: a New Insertion Device Beamline at SOLEIL for Time Resolved Photoelectron Spectroscopy Experiments on Solids and Interfaces. *AIP Conference Proceedings* **2010**, *1234*, 185–188.

(53) Bocquet, F.; Mercurio, G.; Franke, M.; van Straaten, G.; Weiß, S.; Soubatch, S.; Kumpf, C.; Tautz, F. Torricelli: A software to determine atomic spatial distributions from normal incidence x-ray standing wave data. *Comput. Phys. Commun.* **2019**, *235*, 502–513.

(54) Mott, N. F.; Littleton, M. J. Conduction in polar crystals. I. Electrolytic conduction in solid salts. *Trans. Faraday Soc.* **1938**, *34*, 485–499.

(55) Mott, N. F. Conduction in polar crystals. II. The conduction band and ultra-violet absorption of alkali-halide crystals. *Trans. Faraday Soc.* **1938**, *34*, 500–5006.

(56) Citrin, P. H.; Thomas, T. D. X-Ray Photoelectron Spectroscopy of Alkali Halides. *J. Chem. Phys.* **1972**, *57*, 4446–4461.

(57) Mahan, G. D. Photoemission from alkali halides: Energies and line shapes. *Phys. Rev. B* **1980**, *21*, 4791–4803.

(58) Romaner, L.; Heimel, G.; Ambrosch-Draxl, C.; Zojer, E. The Dielectric Constant of Self-Assembled Monolayers. *Adv. Funct. Mater.* **2008**, *18*, 3999–4006.

(59) Iwamoto, M.; Mizutani, Y.; Sugimura, A. Calculation of the dielectric constant of monolayer films on a material surface. *Phys. Rev. B* **1996**, *54*, 8186–8190.

(60) Díaz-Tendero, S.; Borisov, A. G.; Gauyacq, J.-P. Theoretical study of the electronic excited states in ultrathin ionic layers supported on metal surfaces: NaCl/Cu(111). *Phys. Rev. B* **2011**, *83*, 115453.

(61) Chulkov, E.; Silkin, V.; Echenique, P. Image potential states on metal surfaces: binding energies and wave functions. *Surf. Sci.* **1999**, *437*, 330–352.

(62) Jaswal, S.; Sharma, T. Electronic polarisabilities of ions in alkali halide crystals. *J. Phys. Chem. Solids* **1973**, *34*, 509–511.

(63) Le Moal, E.; Müller, M.; Bauer, O.; Sokolowski, M. Misfit driven azimuthal orientation of NaCl domains on Ag(100). *Surf. Sci.* **2009**, *603*, 2434–2444.

(64) Husseen, A.; Le Moal, S.; Oughaddou, H.; Dujardin, G.; Mayne, A.; Le Moal, E. Reaction kinetics of ultrathin NaCl films on Ag(001) upon electron irradiation. *Phys. Rev. B* **2017**, *96*, 235418.

(65) Müller, M.; Ikonomov, J.; Sokolowski, M. Structure of Epitaxial Layers of KCl on Ag(100). *Surf. Sci.* **2011**, *605*, 1090–1094.

(66) Boutboul, T.; Akkerman, A.; Breskin, A.; Chechik, R. Electron inelastic mean free path and stopping power modelling in alkali halides in the 50 eV-10 keV energy range. *J. Appl. Phys.* **1996**, *79*, 6714–6721.

(67) Henke, B. L.; Gullikson, E. M.; Davis, J. X-Ray Interactions: Photoabsorption, Scattering, Transmission, and Reflection at E = 50-30,000 eV, Z = 1-92. *At. Data Nucl. Data Tables* **1993**, *54*, 181–342.

(68) Mahan, G. D. Electron energies of ions in crystals. *Phys. Rev. B* **1980**, *22*, 3102–3106.

(69) Repp, J.; Meyer, G.; Paavilainen, S.; Olsson, F. E.; Persson, M. Scanning Tunneling Spectroscopy of Cl Vacancies in NaCl Films: Strong Electron-Phonon Coupling in Double-Barrier Tunneling Junctions. *Phys. Rev. Lett.* **2005**, *95*, 225503.

Graphical TOC Entry